Interrupted anion-network enhanced Li$^+$-ion conduction in Li$_{3+y}$PO$_4$I$_y$

Sawankumar V. Patel [a], Erica Truong [a], Haoyu Liu [a], Yongkang Jin [a], Benjamin L. Chen [a], Yan Wang [c], Lincoln Miara [c], Ryounghee Kim [d], Yan-Yan Hu [a,b,*]

[a] Department of Chemistry and Biochemistry, Florida State University, Tallahassee, FL 32306, USA
[b] Center of Interdisciplinary Magnetic Resonance, National High Magnetic Field Laboratory, 1800 East Paul Dirac Drive, Tallahassee, FL 32310, USA
[c] Advanced Materials Lab, Samsung Advanced Institute of Technology-America, Samsung Semiconductor, Inc., Cambridge, Massachusetts 02138, USA
[d] Battery Material Lab, Samsung Advanced Institute of Technology, Samsung Electronics Co., Ltd., Suwonsi, Gyeonggi-do 16678, Republic of Korea

ARTICLE INFO

ABSTRACT

For solid-state batteries to outperform the current lithium-ion battery technology in energy density and cost, high-performance solid electrolytes produced using low-cost precursors and scalable processes are the key. In this study, we demonstrate using inexpensive Li$_3$PO$_4$ of low conductivity 10^{-6} mS/cm and turning it into a fast Li$^+$-ion conductor, with an ionic conductivity of ≥ 0.15 mS/cm, by engineering the anion sublattice. I$^-$ anions are used to interrupt the ordered PO$_4^{3-}$ network in Li$_3$PO$_4$, which destabilizes Li$^+$-PO$_4^{3-}$ interaction and liberates Li$^+$-ions with enhanced Li$^+$ mobility as evidenced by NMR relaxometry measurements. The optimal conductivity and activation energy are achieved when PO$_4^{3-}$/I$^-$ =1, in which Li$^+$-ions spend equal time with PO$_4^{3-}$ and I$^-$ on their diffusion paths without being trapped. Tracer-exchange NMR shows that Li$_4$PO$_4$I is more conductive than Li$_{3+y}$PO$_4$I$_y$ when y $\neq$ 1. Further conductivity enhancement is possible by stabilizing pure-phase glassy Li$_4$PO$_4$I. Overall, this study shows an effective and general strategy to significantly enhance ion conduction for creating inexpensive solid electrolytes with high performance.

1. Introduction

All-solid-state batteries (ASSBs) emerge as a promising energy storage technology to potentially replace current rechargeable Li$^+$-ion batteries in the near future [1,2]. Development of solid electrolytes with high ionic conductivity, good electrode-compatibility, and low-temperature synthesis using cost-effective precursors is crucial to reducing the cost of ASSBs [3]. Oxide-, thiophosphate-, and halide-based solid electrolytes have been extensively investigated for ASSBs [2]. Most of these solid electrolytes either require expensive precursors or synthesis at high temperatures or pressures thereby posing challenges for large-scale productions [4,5]. Therefore, high-performance solid electrolytes that can be synthesized under mild conditions with cost-effective precursors are important to the development of ASSBs.

Inexpensive Li$^+$-containing precursors such as lithium phosphates are not highly conductive, due to strong Li$^+$-anion interactions within ordered structures. The arrangement of anions in the sublattice is critical to Li$^+$-ion conduction. Slight alterations in anion substructure can create static and dynamic structural disorder, which significantly impacts ion transport [6–12]. A mixed-anion sublattice that involves multiple anions

has also been shown conducive to enhanced cation conduction, through tuning cation-anion interactions [13]. For example, Malugani et al. studied the AgPO$_3$ – AgI binary system, achieving a 4-fold increase in Ag$^+$-ion conductivity compared with AgPO$_3$ alone [14]. Likewise, lithium glasses composed of LiI and LiPO$_3$ yielded a 3-fold increase in ionic conductivity compared with LiPO$_3$ [15]. Kaus et al., demonstrated that combining Li$_3$PO$_4$ and LiI precursors can produce conductivities up to 1 mS/cm [16]. These materials are usually made via mechanochemical synthesis at room temperature. The high-energy milling process results in the reduction of particle size, efficient mixing of the precursor materials, and generation of new phases which may possess unprecedented properties [17].

Mechanochemical synthesis often generates a mixture of phases, and little is known regarding the mechanism of enhanced Li$^+$-ion conduction in these complex composites. Unraveling Li$^+$-ion transport and identifying the component(s) that are responsible for the observed high ionic conductivities are critical for strategic design and synthesis of cost-effective high-performance solid electrolytes. Therefore, we investigated the Li$_3$PO$_4$-LiI binary system as a representative example to illustrate the origin of fast ion conduction in these mixed-anion systems. A mixed-anion framework of phosphate and iodide was created using

Abbreviations

All-solid-state batteries (ASSBs)
nuclear magnetic resonance (NMR)
ab initio molecular dynamics (AIMD)
X-ray diffraction (XRD)
exchange NMR spectroscopy (EXSY)
High-Temperature (HT)
Low-Temperature (LT)

Li_3PO_4 and LiI as precursors and room-temperature mechanochemical milling. An ionic conductivity of 0.15 mS/cm at room temperature is obtained, which is at least 10^5 times the ionic conductivity of Li_3PO_4, with a significant reduction of activation energy for Li^+-ion transport. Comprehensive phase analysis was carried out using X-ray diffraction (XRD) and solid-state nuclear magnetic resonance (NMR). NMR relaxometry was performed to determine Li^+-ion mobility, and tracer-exchange NMR was used to probe Li^+-ion transport pathways. A new phase, glassy Li_4PO_4I (g-Li_4PO_4I), is identified, which exhibits a mixed PO_4^{3-}-I^- anion framework, shows high Li^+-ion mobility, and is responsible for the observed high ionic conductivity.

2. Experimental

2.1. Synthesis

Lithium iodide (99.9 %, Alfa Aesar) and lithium phosphate (99%, Sigma Aldrich) were dried at 120°C under dynamic vacuum. xLi_3PO_4 − LiI (x = 1, 1.4, or 2) was mixed in a 25-ml zirconia jar with 10-mm zirconia balls. Mechanochemical mixing of Li_3PO_4 and LiI was performed using the SPEX 8000M for 20 hours. The as-milled powder was stored in an argon glovebox. Samples were cold pressed into a pellet for characterization. The density of the pellets is ∼ 2.3 ± 0.2 g/cm³.

2.2. X-ray Diffraction

Powder samples were finely grounded and packed in a zero-background sample holder. Kapton film was used to seal the samples to prevent exposure to humid air. XRD was performed using Rigaku D8 powder diffractometer with Bragg-Brentano geometry at a voltage of 44 kV and a current of 40 mA with Cu-Kα radiation (λ = 1.5406 Å). The data was collected in the 2Θ range of 10° – 80° at a step size of 0.03° with a total acquisition time of 30 minutes.

2.3. Solid-state NMR

^6Li, ^7Li, and ^{31}P Magic-Angle-Spinning (MAS) solid-state NMR experiments were performed using a Bruker Avance-III 500 MHz spectrometer at Larmor frequencies of 73.6 MHz, 194.4 MHz, and 202.4 MHz, respectively. The MAS rate was 24 kHz. Single-pulse ^6Li and ^7Li NMR experiments were performed with π/2 pulse lengths of 4.75 μs and 3.35 μs, respectively. The recycle delays were 1000 s for ^6Li and 20 s for ^7Li. For ^{31}P, a rotor-synchronized spin-echo sequence was employed with a π/2 pulse length of 4.2 μs and a recycle delay of 1000 s. 2D EXchange SpectroscopY (EXSY) NMR experiments were acquired using π/2 and π pulse lengths of 4.75 μs and 9.50 μs, respectively. The EXSY spectra were recorded using 512 t_1 increments and with mixing times of 0.1, 5, and 100 ms. $^{6,7}Li$ and ^{31}P NMR spectra were referenced to $LiCl_{(s)}$ at -1.1 ppm and 85% $H_3PO_{4(l)}$ at 0 ppm, respectively. High-temperature ^7Li NMR measurements were conducted to determine the ion dynamics using the 300 MHz spectrometer at the Larmor frequency of 116 MHz. The inversion recovery pulse sequence was used to determine the variable-temperature T_1 relaxation times. The experiment was

performed between 25 to 110°C. Tracer exchange NMR was carried out by assembling a symmetric cell with the $Li_{3+y}PO_4I_y$ pellet sandwiched by two pieces of ^6Li-foil, and then a biased electric potential was applied to this symmetric cell made of $^6Li|Li_{3+y}PO_4I_y|^6Li$ to drive $^6Li^+$-ions diffuse from ^6Li-foil into $Li_{3+y}PO_4I_y$ which contains natural-abundance Li, *i.e.*, 92.4 mol% ^7Li and 7.6 mol% ^6Li. The symmetric cell was electrochemically cycled for 50 and 110 times with a current density of 10 μA/cm². Another symmetric cell made of a $Li_{3+y}PO_4I_y$ pellet sandwiched by two pieces of Li-foil of natural-abundance lithium ($^{nat.}Li$) was assembled to serve as a control reference.

2.4. Electrochemical measurements

The ionic conductivity of xLi_3PO_4 - LiI composite electrolytes was determined based on AC impedance spectroscopy acquired using a Gamry Analyzer Reference 600+ within a frequency range of 5 MHz to 1 Hz. Indium foils were pressed onto the surface of the pellet as blocking electrodes and the pellet was placed in a custom-built cylindrical cell. Variable-temperature impedance measurements were conducted using the CSZ Microclimate chamber within the temperature range of 20 to 100°C, over frequencies from 5 MHz to 1 Hz with an applied voltage of 10 mV. Electronic conductivity measurements were conducted by subjecting the pellets under a constant DC polarization of 3 V.

2.5. DFT calculation

All the density functional theory (DFT) calculations were performed using Vienna *ab initio* simulation package (VASP) based on projector-augmented-wave method [18,19] with Perdew-Burke-Ernzerh of generalized-gradient approximation (PBE-GGA) [20]. Pristine structure of Li_4PO_4I was generated by replacing Ag^+ with Li^+ in the structure of Ag_4PO_4I retrieved from Inorganic Crystal Structure Database (ICSD No. 245791) [21]. Then the atom positions and the shape of the unit cell were relaxed. After the structure of crystalline-phase Li_4PO_4I was determined, *ab initio* molecular dynamics (AIMD) simulation was used to raise the temperature to 1000 K, which was maintained for 80 ps before the system was quenched to 0 K by allowing structure to relax. A glassy phase of Li_4PO_4I was found by this process. Canonical ensemble was chosen for AIMD simulations with a time step of 2 fs. AIMD at different temperatures (500 K, 600 K, 700 K, 800 K, 1000 K) with a total simulation time of 240 ps was performed to obtain diffusivity rates. The diffusivity analysis and conductivity/activation energy calculations [22] were performed using pymatgen. The isotropic chemical shifts of relaxed structures were calculated using the perturbation theory (linear response) [23,24]. The calibration factor of ^6Li (+89 ppm) was estimated from the difference between the experimental and calculated isotropic shift of Li, which was validated in our previous work [6].

3. Result and discussion

3.1. Synthesis and structure characterization

Li_3PO_4 crystal structure consists of two known polymorphs as shown in Fig. 1a. The low-temperature phase β-Li_3PO_4 (Pmn2₁) transforms to γ-Li_3PO_4 (Pnma) at 500°C [26,27]. β-Li_3PO_4 consists of an ordered arrangement of PO_4^{3-} with all the tetrahedra aligned in the same direction whereas γ-Li_3PO_4 is formed by alternating the orientation of PO_4^{3-} tetrahedra in opposite ways. The lattice experiences a volume expansion of ∼ 1.4 % for the β- → γ-Li_3PO_4 transformation. β-Li_3PO_4 in the glassy phase exhibits a room-temperature ionic conductivity of 10^{-9} – 10^{-7} S/cm, whereas, the crystalline form exhibits an ionic conductivity of 10^{-17} S/cm which is 10-fold lower than the glassy phase [25, 28]. γ-Li_3PO_4 with a disordered anion sublattice (Fig. 1a) shows further improved ionic conductivity to 10^{-7} – 10^{-5} S/cm (Fig. 1c). This denotes how structural changes, particularly in the anion network, can significantly influence ion conduction. High activation energy barrier for ion
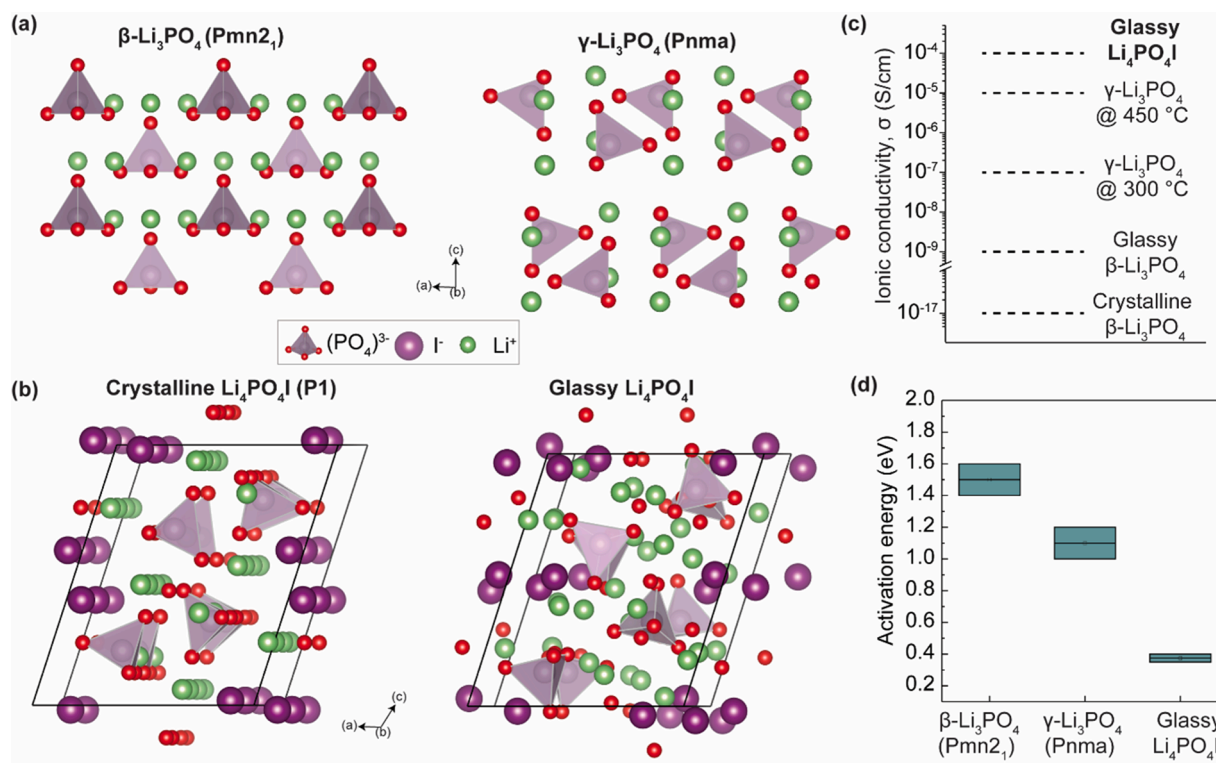
Fig. 1. Disorder in PO_4^{3-} sublattice correlates with enhanced Li^+-ion conduction in Li_3PO_4 polymorphs and its derivatives. (a) Structural illustration of Li_3PO_4 polymorphs and Li_4PO_4I. Crystal structures of β-Li_3PO_4 and γ-Li_3PO_4, representing the ordered and disordered arrangement of the PO_4^{3-} network, respectively. (b) Structures of Li_4PO_4I in the crystalline and glassy forms. (c) Comparison of experimental ionic conductivities of Li_3PO_4 polymorphs with computed conductivity of g-Li_4PO_4I. The ionic conductivity of γ-Li_3PO_4 was reported at 300 and 450°C. [25] (d) Comparison of the activation energy (E_a) for Li^+-ion migration in β-Li_3PO_4, γ-Li_3PO_4, and glassy Li_4PO_4I. The values of β-Li_3PO_4 and γ-Li_3PO_4 are from literature reports, showing activation energy of (1.6 - 1.4 eV) [26] and (1.2 - 1.0 eV) [25], respectively. The Li^+-ion conductivity and activation energy (E_a) for glassy Li_4PO_4I are obtained from AIMD simulations (Fig.. S1a-f).

conduction (>1 eV) is also found in highly ordered Li_3PO_4 as shown in Fig. 1d. In order to further examine the effects of disordered anion sublattice on Li^+-ion conduction, computational work is carried out on Li_4PO_4I, in which the PO_4^{3-} network is interrupted by I^- anions. The Li_4PO_4I structure was derived by substituting Ag^+ with Li^+ in the $Ag_4(PO_4)I$ structure retrieved from the Inorganic Crystal Structure Database (ICSD No. 245791) [21]. Both crystalline and glassy phases of Li_4PO_4I are shown in Fig. 1b. The disordered (glassy) structures of Li_4PO_4I are obtained by elevating the temperature to 1000 K and subsequently quenching it to 0 K in AIMD, as described in the experimental section. AIMD simulations were carried out to investigate the Li^+-ion diffusivity. Fig. S1a-e presents the lithium mean squared displacement (MSD) as a function of time at 500, 600, 700, 800, and 1000 K within a representative disordered structure shown in Fig. 1c, revealing comparable fast Li^+-ion diffusion in all three dimensions. From the computed Arrhenius plot as shown in Fig. S1f, the activation energy for Li^+-ion transport in glassy Li_4PO_4I is determined to be 0.37 eV, which is the lowest in comparison to β-Li_3PO_4 and γ-Li_3PO_4 (Fig. 1d). It is worth noting that the ordered structure of Li_4PO_4I is not particularly conductive (Fig. S2 a-b). This suggests that in the synthesis of highly conductive Li_4PO_4I, temperature needs to be controlled as not to crystallize the structure. The same heating-quenching procedure was also applied to β-Li_3PO_4 and γ-Li_3PO_4 to generate glassy phases for AIMD simulations. No appreciable diffusion was observed within 240 ps even at 1000 K as shown in Fig. S2c-d, indicating that I^- anions are critical for the observed fast Li^+-ion conduction in the glassy Li_4PO_4I.

Synthesis of the computationally predicted conductive g-Li_4PO_4I was attempted via high-energy mechanochemical ballmilling of Li_3PO_4 and LiI as described in the experimental section. Fig. 2a shows a schematic of the synthesis procedure. Crystalline phase analysis of the as-milled LiI, Li_3PO_4, and 1.4Li_3PO_4–LiI is performed based on the powder X-ray

diffraction (pXRD) patterns shown in Fig. 2b. The as-milled precursor samples of LiI and Li_3PO_4 exhibit broad Bragg reflections due to particle size reduction during the milling process. Detailed refinement of the pXRD patterns is presented in Fig. S3. The as-milled LiI sample maintains the rock-salt structure (Fm-3m) and shows a hydrate phase LiI·H_2O (Pm-3m). Rietveld analysis revealed a phase fraction of 37.9 and 62.1 wt.% of the LiI·H_2O and LiI phases, respectively (Fig. S4). The as-milled Li_3PO_4 also preserves the long-range structure of β-Li_3PO_4 (Pmn2₁), albeit nano-sized. The pXRDs of xLi_3PO_4 – LiI only show Bragg reflections of residual crystalline precursors, LiI and LiI·H_2O phases, while the major phases are invisible due to lack of long-range structural order. Therefore, high-resolution solid-state NMR experiments are performed to capture highly disordered phases.

High-resolution [6]Li NMR is used to determine the local structures of chemical phases formed in the xLi_3PO_4 – LiI samples. Fig. 3a shows the [6]Li NMR of as-milled LiI, Li_3PO_4, and 1.4Li_3PO_4 – LiI. The spectrum of the as-milled LiI displays two resonances assigned to the LiI and LiI·H_2O phases resonating around -4.45 and -4.40 ppm, respectively. The as-milled LiI contains ~ 65% of LiI and ~35% of LiI·H_2O based on NMR and powder XRD characterizations (Table S1). [6]Li NMR of Li_3PO_4 displayed two resonances of Li_1 and Li_2 at 0.14 and 0.41 ppm, respectively, which are attributed to the two different Li sites within the β-Li_3PO_4 phase [29]. The [6]Li NMR spectrum of 1.4Li_3PO_4 – LiI exhibits resonances from minor residual LiI and LiI·H_2O. In addition, a broad resonance centered around -0.7 ppm is attributed to g-Li_4PO_4I, confirmed by DFT NMR calculations (Fig. 3c). The -0.7 ppm resonance lies at the weighted average of Li_3PO_4 (0.32 ppm) and LiI (-4.45 ppm), indicating that mobile Li^+-ions statistically spend equal amount of time close to PO_4^{3-} and to I^- anions, in other words, no trapping of Li^+-ions by either PO_4^{3-} or I^- anions.

Apart from g-Li_4PO_4I, a large amount of $Li_{3+y}PO_4I_y$ (y < 1) is also
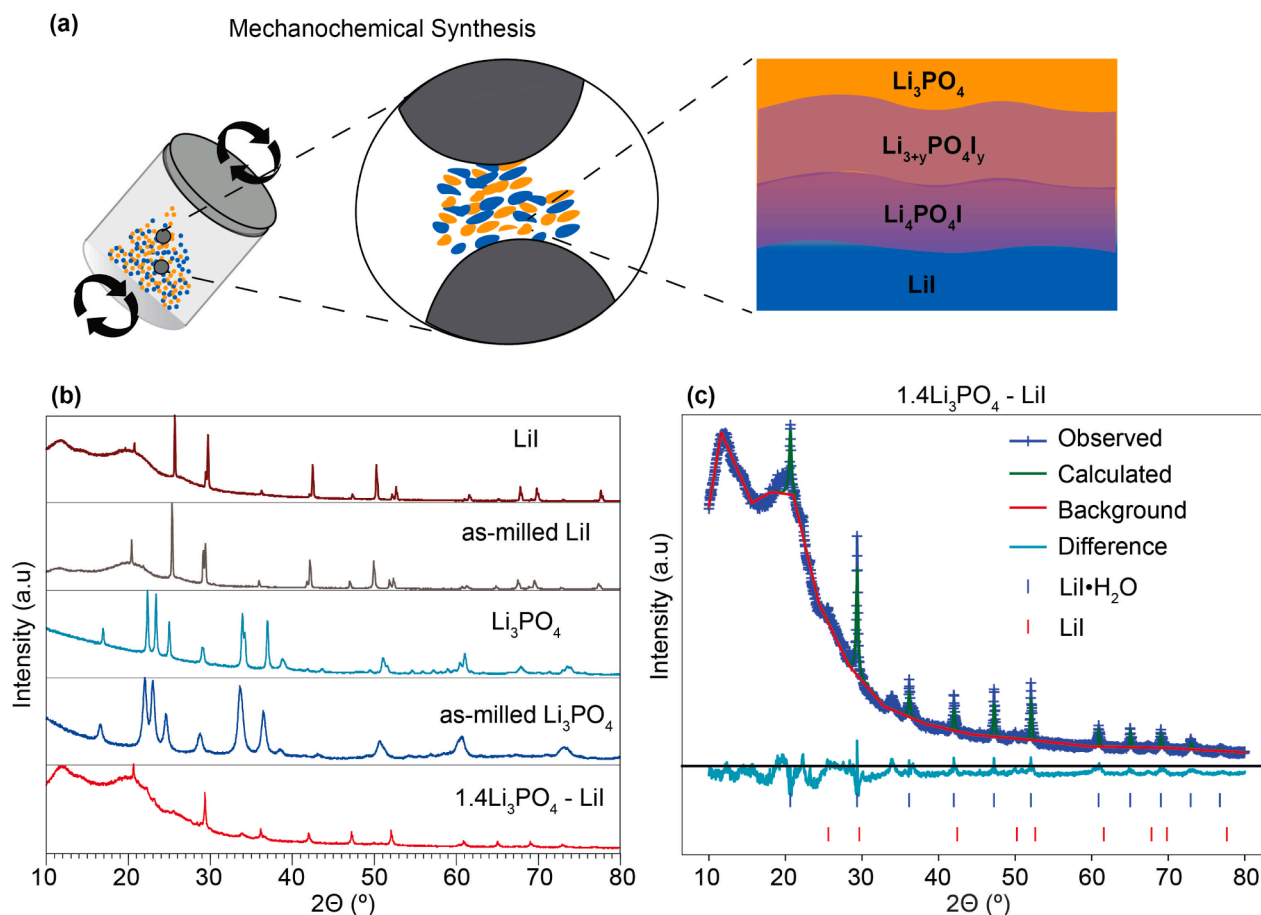
Fig. 2. Synthesis and crystalline-phase analysis of the Li$_3$PO$_4$–LiI systems. (a) Schematic representation of room-temperature synthesis via mechanochemical high-energy milling, resulting in Li$^+$-conductive, largely disordered phases later confirmed as Li$_{3+y}$PO$_4$I$_y$ (0 ≤ y ≤ 0.08) and g-Li$_4$PO$_4$I. (b) Powder X-ray diffraction (pXRD) of the dry and as-milled Li$_3$PO$_4$ and LiI precursors, and as-milled 1.4Li$_3$PO$_4$ – LiI. (c) Rietveld analysis of pXRD on 1.4Li$_3$PO$_4$ – LiI, revealing the presence of LiI (Fm-3m) and LiI·H$_2$O (Pm-3m) as the major residual crystalline phases.

formed but not observed in pXRD due to lack of long-range structural order. The ^{6}Li NMR shift of the Li$_{3+y}$PO$_4$I$_y$ phase in the xLi$_3$PO$_4$–LiI samples moves upfield linearly upon increasing the LiI amount (Fig. S5), an indicator of a solid solution behavior. A calibration curve of ^{6}Li NMR shifts for Li$_{3+y}$PO$_4$I$_y$ is generated based on experimental ^{6}Li NMR of Li$_3$PO$_4$, LiI, and Li$_4$PO$_4$ I (Fig. S6). The shifts of Li$_1$ and Li$_2$ NMR resonances in xLi$_3$PO$_4$ – LiI are then used to determine the y values in Li$_{3+y}$PO$_4$I$_y$ (Fig. 3d). Li$_{3.06}$PO$_4$I$_{0.06}$ is formed in the sample of 1.4Li$_3$PO$_4$ – LiI. Li$_{3.06}$PO$_4$I$_{0.06}$ displays a slightly preferred occupancy of the Li$_2$ sites over Li$_1$ compared with Li$_3$PO$_4$ (Fig. S6). The difference in Li occupancy between Li$_{3.06}$PO$_4$I$_{0.06}$ and Li$_3$PO$_4$ also implies that Li$_{3.06}$PO$_4$I$_{0.06}$ is distinct from Li$_3$PO$_4$, albeit the small amount of LiI incorporation into the structure.

^{7}Li NMR relaxometry was utilized to study Li$^+$-ion mobility in Li$_3$PO$_4$, LiI, and Li$_{3+y}$PO$_4$I$_y$. According to the Bloembergen, Purcell, and Pound (BPP) model [30], T$_1$ relaxation time is a function of motional rate (1/τ_c), as shown in Equation (1) [6,9,31].

$$\left(\frac{1}{T_1}\right) = \frac{3\mu_o^2\gamma^4\hbar^2}{10r_0^6}\left[\frac{\tau_c}{1+(\omega_o\tau_c)^2} + \frac{4\tau_c}{1+4(\omega_o\tau_c)^2}\right] \tag{1}$$

Where γ is the magnetogyric ratio, μ$_o$ is the vacuum permeability, $\hbar$ is the reduced Planck constant, r$_o$ is the interatomic distance, and ω$_o$ is the Larmor frequency. In the fast-motion regime (ω$_o$τ$_c$ <<1), T$_1$ increases with increasing motional rate while in the slow-motion regime (ω$_o$τ$_c$ >>1), T$_1$ decreases with increasing motional rate. To determine the motional regime, variable-temperature ^{7}Li NMR T$_1$ values of the 1.4Li$_3$PO$_4$ – LiI sample are determined in the temperature range of 20-

120 °C. As shown in Fig. 4a, faster ion motion at increased temperatures results in smaller T$_1$ values, indicating Li$^+$-ion motion in this material lies in the slow-motion regime of the BPP model. Fig. 4b shows the results of ^{7}Li NMR T$_1$ measurements on Li$_3$PO$_4$, LiI, and Li$_{3+y}$PO$_4$I$_y$, which reveal relatively large T$_1$ values of 4.7 and 10.1 s for LiI and Li$_3$PO$_4$, respectively. On the other hand, Li$_{3.06}$PO$_4$I$_{0.06}$ and g-Li$_4$PO$_4$I in 1.4Li$_3$PO$_4$ – LiI exhibit shorter T$_1$ values of 3.5 s and 1.7 s, respectively, implying higher Li$^+$-ion mobility than the precursors Li$_3$PO$_4$ and LiI. Overall, g-Li$_4$PO$_4$I shows the shortest T$_1$, thus the highest Li$^+$-ion mobility.

The relative spatial proximity of Li$_{3+y}$PO$_4$I$_y$ and LiI in 1.4Li$_3$PO$_4$ – LiI is determined with 2D ^{7}Li exchange NMR spectroscopy (EXSY). In 2D EXSY NMR, spin exchange is predominantly driven by dipolar coupling interactions. The dipolar coupling constant d$_{ij}$, as shown in Equation (2), is strongly distance (r_{ij}^3) dependent, [32] where r$_{ij}$ is the distance between spins i and j, γ$_i$ and γ$_j$ refer to the magnetogyric ratios of the spins i and j, respectively, $\hbar$ is the reduced Planck's constant, and θ$_{ij}$ is the angle between the internuclear vector $\overrightarrow{r_{ij}}$ and $\overrightarrow{B_0}$.

$$d_{ij} = -\frac{\mu_0}{4\pi}\frac{\gamma_i\gamma_j\hbar^2}{r_{ij}^3}\frac{1}{2}\left(3cos^2\theta_{ij}-1\right) \tag{2}$$

A diagonal peak in the 2D EXSY NMR signifies self-correlation of ^{7}Li spins within a particular phase, while a cross peak (off-diagonal peak) indicates interaction of spins from two different chemical phases through transfer of magnetization. The intensity of cross peaks is mainly dictated by the spatial proximity of two phases and time period provided
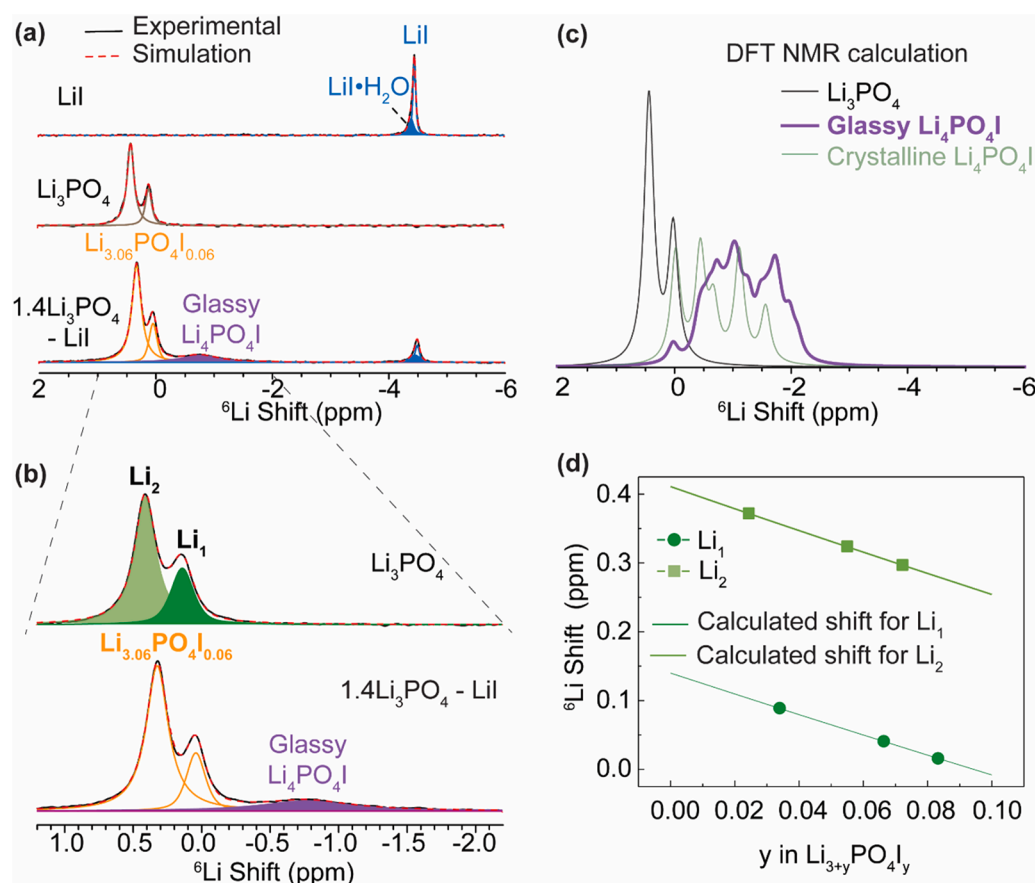
Fig. 3. Phase determination of $Li_{3+y}PO_4I_y$ in the $1.4Li_3PO_4 - LiI$ sample. (a) ^6Li NMR of as-milled LiI, Li_3PO_4, and $1.4Li_3PO_4 - LiI$ samples. As-milled LiI shows the $LiI \cdot H_2O$ phase whereas Li_3PO_4 shows two resonances representing two distinct Li sites. As-milled $1.4Li_3PO_4 - LiI$ displays NMR resonances from LiI, $LiI \cdot H_2O$, $Li_{3.06}PO_4I_{0.06}$, and $g-Li_4PO_4I$. (b) Zoomed in ^6Li NMR of as-milled Li_3PO_4 and $1.4Li_3PO_4 - LiI$ focusing on the $Li_{3.06}PO_4I_{0.06}$ phase. (c) DFT ^6Li NMR calculations of Li_3PO_4 and Li_4PO_4I phases. (d) Calculated calibration curve of changes in chemical shift due to the addition of LiI into bulk Li_3PO_4, which helps to determine the phase composition of $Li_{3.06}PO_4I_{0.06}$.
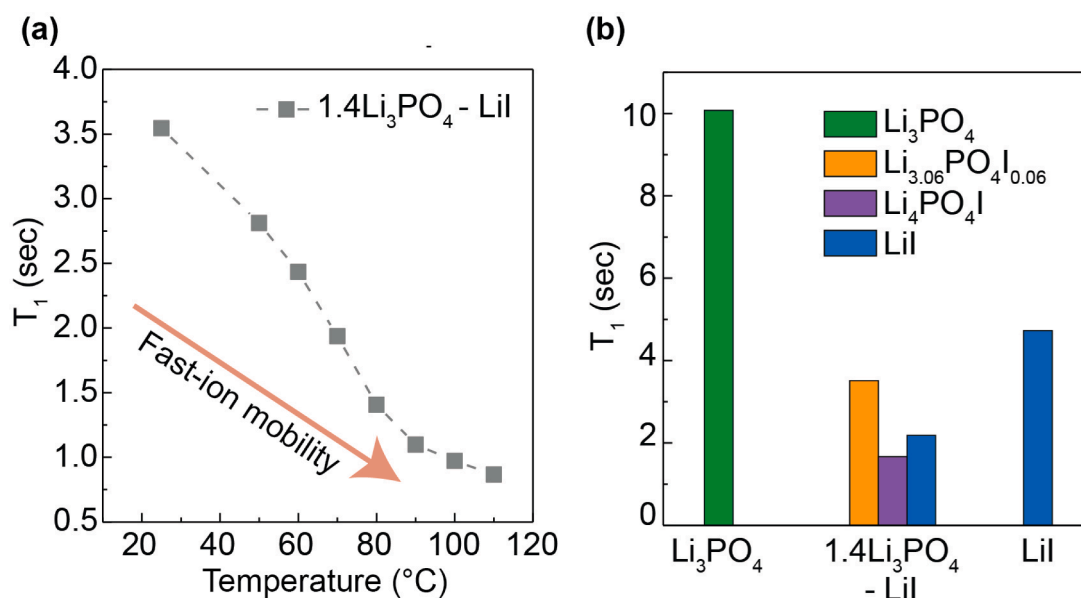

Fig. 4. NMR relaxometry for probing Li^+-ion mobility in $Li_{3+y}PO_4I_y$ and LiI. (a) Variable-temperature ^7Li NMR T_1 relaxation measurements on $1.4Li_3PO_4 - LiI$. As Li^+-ion mobility increases with temperature, the measurements suggest that shorter T_1 values correlate with faster Li^+-ion motion in this temperature range of 20-120 °C. (b) ^7Li NMR T_1 relaxation times of Li_3PO_4, $g-Li_4PO_4I$, $Li_{3.06}PO_4I_{0.06}$, and LiI. The precursors Li_3PO_4 and LiI have longer T_1 compared to $Li_{3+y}PO_4I_y$, indicating faster Li^+-ion mobility in $Li_{3+y}PO_4I_y$. $g-Li_4PO_4I$ displays the fastest Li^+-ion mobility of all.

for the magnetization transfer to take place, *i.e.*, mixing time. Strong cross peaks within a short mixing time suggest close spatial proximity of two chemical phases. Fig. 5 shows the ^7Li 2D EXSY NMR spectra acquired with mixing times of 0.1, 5, and 100 ms. During the short mixing time of 0.1 ms, only three diagonal peaks are observed at ~ 0, -0.7, and -4.5 ppm signifying minimal polarization transfer among the ^7Li spins from the $Li_{3.06}PO_4I_{0.06}$, $g-Li_4PO_4I$, and $LiI/LiI \cdot H_2O$ phases. The cross peaks (marked in red) between LiI and $g-Li_4PO_4I$ phases at (-4.5 ppm,

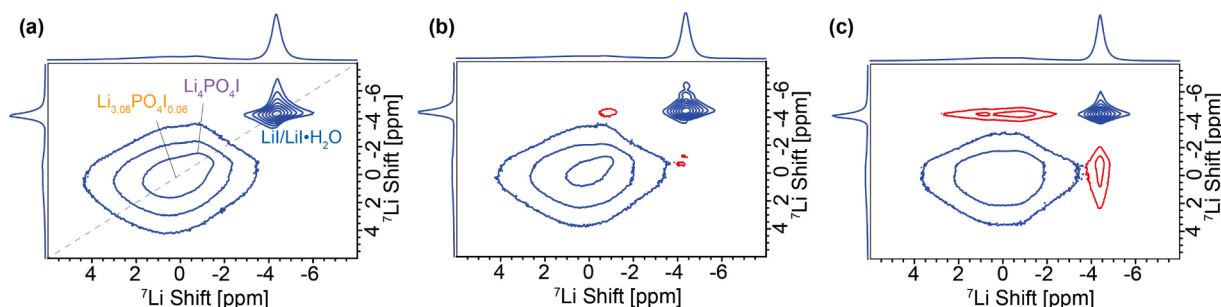**Fig. 5.** Spatial proximity of phases in 1.4Li$_3$PO$_4$ – LiI determined by 2D ^{7}Li EXSY NMR with mixing times of (a) 0.1 ms, (b) 5 ms, and (c) 100 ms. The emergence of off-diagonal (or cross peaks, shown in red) at longer mixing times (5 and 100 ms) reveal g-Li$_4$PO$_4$I, LiI, LiI·H$_2$O and Li$_{3.06}$PO$_4$I$_{0.06}$ are close in space on the nanoscale.

-0.7 ppm) emerge first at a mixing time of 5 ms while those between LiI and Li$_{3.06}$PO$_4$I$_{0.06}$ phases at (-4.5 ppm, 0.2 ppm) only become prominent at a longer mixing time of 100 ms, as shown in Fig. 5b and 5c. This indicates that the g-Li$_4$PO$_4$I phase is at the interface of LiI·H$_2$O/LiI and Li$_{3.06}$PO$_4$I$_{0.06}$ phases.

High-resolution ^{31}P NMR is employed to understand the local structural changes in the phosphate "PO$_4^{3-}$" network. Fig. 6a displays the ^{31}P NMR spectra of pristine Li$_3$PO$_4$, as-milled Li$_3$PO$_4$, and 1.4Li$_3$PO$_4$ – LiI. All ^{31}P NMR resonances fall between 6-12 ppm, suggesting an isolated form of PO$_4^{3-}$ with no bridging O [33–35]. Pristine β-Li$_3$PO$_4$ displays two resonances at 10.2 and 9.7 ppm, which are attributed to the crystalline [β-PO$_4^{3-}$(C)] and glassy Li$_3$PO$_4$ [β-PO$_4^{3-}$(A)], respectively [33]. The as-milled Li$_3$PO$_4$ exhibits an additional resonance at 9.0 ppm, which is assigned to the glassy γ"-Li$_3$PO$_4$ phase. ^{31}P NMR studies performed on Li$_3$PO$_4$ by Snyder et. al. revealed an upfield shift of high-temperature (HT) - γ-Li$_3$PO$_4$ compared to the low-temperature (LT)

- β-Li$_3$PO$_4$ [35]. The major difference in β vs. γ-Li$_3$PO$_4$ lies in the PO$_4^{3-}$ anion packing. As shown in Fig. 6d, the PO$_4^{3-}$ in β-Li$_3$PO$_4$ are packed in an ordered arrangement with all PO$_4^{3-}$ tetrahedra pointing to the same direction, while in γ-Li$_3$PO$_4$, some PO$_4^{3-}$ tetrahedra point to the opposite direction compared to the rest. High energy ball milling of Li$_3$PO$_4$ yields the more disordered γ"-PO$_4^{3-}$(A) network. Incorporation of LiI into Li$_3$PO$_4$ engenders further interruption of the already disordered PO$_4^{3-}$(A) network, manifested in a new ^{31}P NMR resonance shifting further upfield to 8.44 ppm which is assigned to Li$_4$PO$_4$I. DFT NMR calculations show that the glassy Li$_4$PO$_4$I shifts upfield in comparison with the Li$_3$PO$_4$ phase as shown in Table S3. Quantification of the local PO$_4^{3-}$ structures observed in ^{31}P NMR is presented in Fig. 6b; ballmilling Li$_3$PO$_4$ mainly converts [β-PO$_4^{3-}$(C)] to [γ"-PO$_4^{3-}$(A)] and I$^-$ can be incorporated into both the [β-PO$_4^{3-}$(A)] and [γ"-PO$_4^{3-}$(A)] networks but not into [β-PO$_4^{3-}$(C)]. Concomitant to the increased interruption of the PO$_4^{3-}$ network, significant peak narrowing of the ^{31}P NMR resonance from
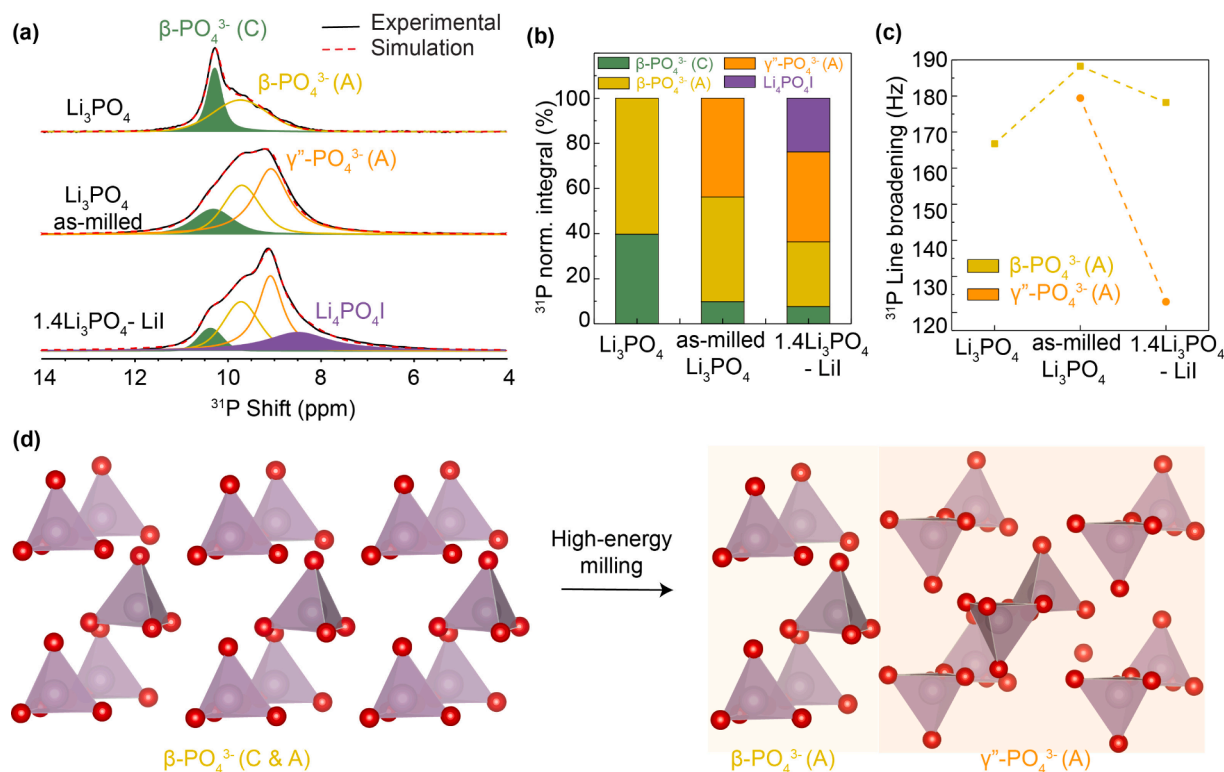

Fig. 6. Characterization of the phosphate anion framework in Li$_3$PO$_4$ and Li$_{3+y}$PO$_4$I$_y$ with ^{31}P NMR. (a) ^{31}P MAS NMR of 1.4Li$_3$PO$_4$ – LiI and Li$_3$PO$_4$. β-Li$_3$PO$_4$ is composed of both crystalline [β-PO$_4^{3-}$(C)] and glassy [β-PO$_4^{3-}$(A)] with distinct NMR resonances. As-milled Li$_3$PO$_4$ results in the formation of glassy [γ"-PO$_4^{3-}$(A)]. Addition of LiI in (1.4Li$_3$PO$_4$ – LiI) causes local structural changes in the [γ"-PO$_4^{3-}$(A)] framework and formation of Li$_4$PO$_4$I. (b) ^{31}P NMR areal integral of the various PO$_4^{3-}$ resonances, revealing evolution of the PO$_4^{3-}$ structures. (c) Comparison of the line broadening between [β-PO$_4^{3-}$(A)] and [γ"-PO$_4^{3-}$(A)] resonances. Addition of LiI results in significant peak narrowing of γ"-PO$_4^{3-}$(A), suggesting enhanced PO$_4^{3-}$ mobility. (d) Arrangement of β-PO$_4^{3-}$(A) and γ"-PO$_4^{3-}$(A) anion frameworks. A and C represent glassy and crystalline phases, respectively.

[γ''-PO_4^{3-}(A)] is observed upon LiI addition as shown in Fig. 6c, indicating increased PO_4^{2-} anion motion. Qualitative ^{31}P NMR relaxation measurements (Fig. S7) reveal that the ^{31}P NMR resonance of Li_4PO_4I has the shortest T_1 thus the PO_4^{3-} in Li_4PO_4I rotates the fastest. The above data suggests that incorporation of I^- into the PO_4^{3-} sublattice leads to both static and dynamic disorder of the PO_4^{2-} anions and the latter may assist Li^+-ion transport [36].

Additionally, ^{127}I NMR is utilized to determine the iodide local environments. As shown in Fig. S8, pristine LiI and as-milled LiI display a sharp symmetric peak resonating at 387 ppm, signifying I^- in a cubic rock-salt structure of high symmetry. ^{127}I NMR resonance of $1.4Li_3PO_4$–LiI shows an upfield change in shift with an asymmetric line shape, suggesting a distorted local chemical environment of I^- anions and successful incorporation of I^- into the PO_4^{3-} network in Li_4PO_4I.

3.2. Ion Conduction

Ionic conductivities of $Li_{3+y}PO_4I_y$ are determined with electrochemical impedance spectroscopy (EIS). Fig. S11 shows that $Li_{3+y}PO_4I_y$ ($Li_{3.06}PO_4I_{0.06}$ and g-Li_4PO_4I) gives a room-temperature ionic conductivity of 0.15 mS/cm, which is two orders of magnitude greater than that of LiI (10^{-3} mS/cm) and at least five orders of magnitude greater than that of Li_3PO_4 ($< 10^{-6}$ mS/cm) (Fig. S9). Fig. 7 shows the temperature dependence of ionic conductivities within the temperature range of 25 – 100 °C and the activation energy is determined to be 0.54 eV. Nyquist plots were fitted using the equivalent circuit model to determine the bulk impedance (Fig. S13). Conductivity was determined using Equation 3, where l is the thickness of the pellet, A is the area of the blocking electrode, and Ω is the impedance. The electronic conductivity is estimated to be relatively low, 1×10^{-4} mS/cm (Fig. S10).

$$\sigma = \frac{l}{A \times \Omega} \tag{3}$$

3.3. Ion transport mechanism

Li^+-ion transport pathways within $Li_{3+y}PO_4I_y$ are investigated with $^6Li \rightarrow {}^7Li$ tracer-exchange NMR. This technique has been utilized by Zheng et al., for studying Li^+-ion transport pathways within composite electrolytes.[32] On their diffusion pathways, $^6Li^+$-ions from ^6Li-foil will exchange with ^7Li in $Li_{3+y}PO_4I_y$, leaving a trace of their paths. Fig. 8a displays the ^6Li NMR of the pristine and tracer-exchanged $Li_{3+y}PO_4I_y$

pellets against $^{nat.}Li$ or ^6Li electrodes. The pristine sample presents four ^6Li NMR resonances assigned to LiI, LiI·H_2O, $Li_{3.06}PO_4I_{0.06}$, and Li_4PO_4I. Electrochemical cycling against ^6Li or $^{nat.}Li$ electrodes results in further conversion of LiI and LiI·H_2O phases to Li_4PO_4I and $Li_{4.3}PO_4I_{1.3}$ with resonances at -0.7 and -1.5 ppm, respectively. The composition of the $Li_{4.3}PO_4I_{1.3}$ phase was determined based on the experimental ^6Li chemical shift at -1.5 ppm and the calibration curve (Fig. S6). Quantification of the Li components is presented in Fig. 8b. Compared with the pristine and control sample ($^{nat.}Li$), the $Li_{3+y}PO_4I_y$ samples cycled against ^6Li electrodes show significant growth of the ^6Li NMR resonance from Li_4PO_4I. Quantitative analysis of ^6Li enrichment in $Li_{3.06}PO_4I_{0.06}$, Li_4PO_4I, and $Li_{4.3}PO_4I_{1.3}$ after $^6Li \rightarrow {}^7Li$ tracer exchange is presented in Fig. 8c. The ^6Li-enrichment in the $Li_{3.06}PO_4I_{0.06}$ phase is minimal, while that in the Li_4PO_4I and $Li_{4.3}PO_4I_{1.3}$ phases is significant, especially in Li_4PO_4I. With this tracer-exchange NMR approach, higher ^6Li-enrichment of a specific chemical phase implies that Li^+-ions more frequently visit that particular phase. Therefore, the results in Fig. 8c and Fig. S12 suggest that Li^+-ions prefer to diffuse through the Li_4PO_4I and $Li_{4.3}PO_4I_{1.3}$, instead of $Li_{3.06}PO_4I_{0.06}$.

Therefore, multinuclear and multi-dimensional high-resolution NMR combined with DFT NMR calculations have yielded a structural model of g-Li_4PO_4I formed at the interface of Li_3PO_4 and LiI. Li_4PO_4I shows significantly enhanced Li^+-ion mobility compared with Li_3PO_4 and LiI, due to increased entropy in the anion network and no trapping of Li^+ by either PO_4^{3-} or I^- anions. Li_4PO_4I is responsible for the observed several orders of magnitude increase in ionic conductivity of $Li_{3+y}PO_4I_y$, according to tracer-exchange NMR analysis. Based on these insights, extensive effort has been invested in attempts to increase the content of g-Li_4PO_4I in $Li_{3+y}PO_4I_y$ to further improve the experimental ionic conductivity. Varying the precursor compositions (Fig. S4) or synthesis approach has led to little success. The formation of less conductive competing phases ($Li_{3+y}PO_4I_y$, y≠1) is hard to eliminate.

4. Conclusion

$Li_{3+y}PO_4I_y$ is formed by combining Li_3PO_4 and LiI at room temperature, which exhibits an ionic conductivity of 0.15 mS/cm, several orders of magnitude higher than either of the parent materials. Structural and compositional analyses reveal that $Li_{3.06}PO_4I_{0.06}$ and g-Li_4PO_4I are the new phases, which show increased entropy in the anion network and varied Li occupancies. In particular, g-Li_4PO_4I formed at the interface of Li_3PO_4 and LiI exhibits much higher Li^+-ion mobility, compared with

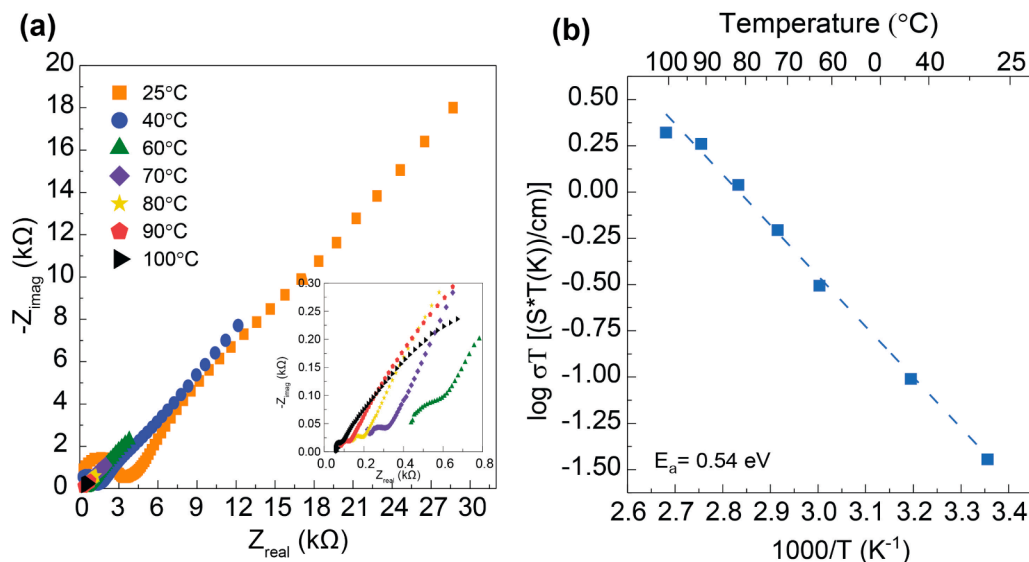**Fig. 7.** Li^+-ion conduction properties of $Li_{3+y}PO_4I_y$ formed in $1.4Li_3PO_4$-LiI obtained with variable-temperature electrochemical impedance spectroscopy in the temperature range of 25-100°C. (a) the Nyquist plots. (b) the Arrhenius plot. The activation energy is determined to be 0.54 eV.
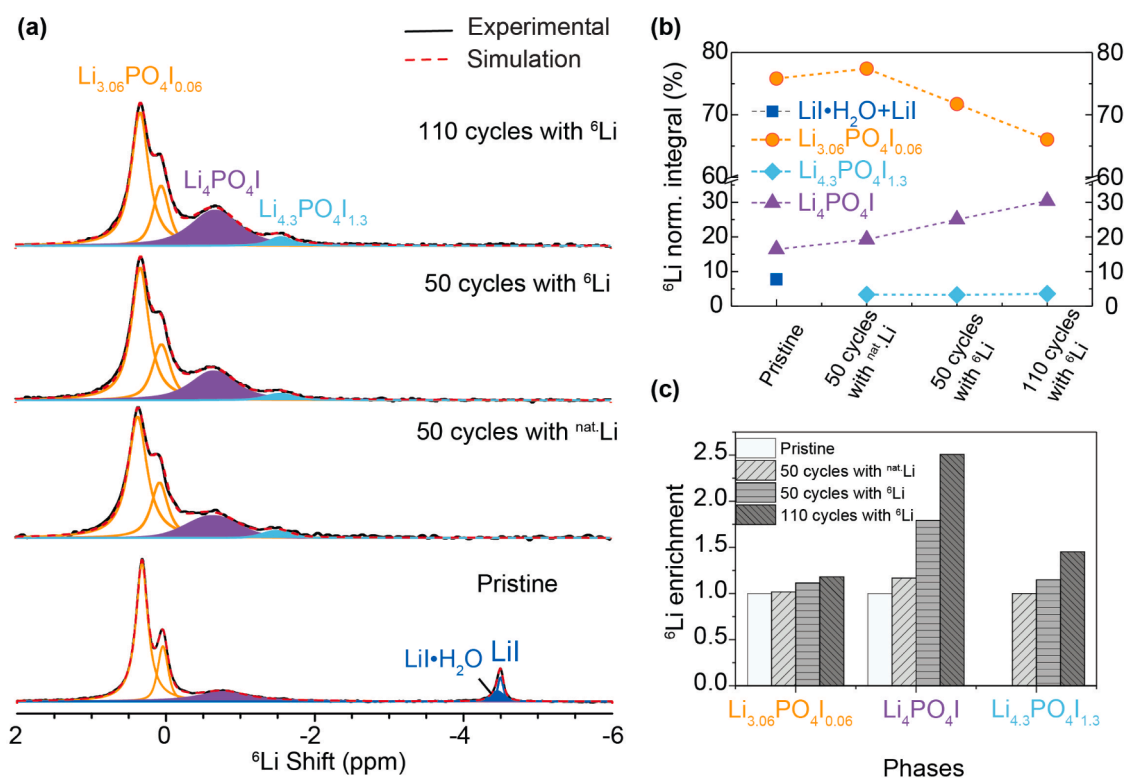
Fig. 8. Li^+-ion transport pathways in $Li_{3+y}PO_4I_y$ determined using $^6Li \rightarrow ^7Li$ tracer-exchange NMR. (a) ^6Li NMR spectra of pristine and cycled $Li_{3+y}PO_4I_y$ using the natural-abundance (^{nat}Li) and ^6Li-enriched lithium metal electrodes, respectively. Electrochemical cycling reveals the disappearance of $LiI/LiI \cdot H_2O$, which is converted to Li_4PO_4I and the iodide-rich interphase $Li_{4.3}PO_4I_{1.3}$ phase. (b) Quantification of ^6Li amount in different phases upon cycling with (^{nat}Li) and ^6Li electrodes. (c) ^6Li NMR areal integrals of the pristine *vs.* cycled samples, revealing the preference of Li^+-ions to diffuse through the Li_4PO_4I phase.

Li_3PO_4, LiI, and $Li_{3.06}PO_4I_{0.06}$. The high Li^+-ion mobility is attributed to the interrupted PO_4^{3-} network by I^- and no trapping of Li^+-ions by either PO_4^{3-} or I^-. Traer-exchange NMR suggests that g-Li_4PO_4I is responsible for the observed high ionic conductivity. This work provides insights into how to tune anion sublattice for enhanced Li^+-ion transport. A balanced interaction between Li^+-ions and all anions is critical to avoid local trapping of active charge carriers; this applies to both glassy and crystalline materials. Systematic computational studies on anion compatibility and Li^+-anion interactions can be beneficial to efficient discovery of new mixed-anion fast-ion conductors.

CRediT authorship contribution statement

The manuscript was written through contributions of all authors. All authors have given approval to the final version of the manuscript. **Sawankumar V. Patel** and **Erica Truong**: contributed equally on tsample synthesis, data acquisition and analysis, and manuscript preparation. **Haoyu Liu**: DFT calculations, data analysis, and manucript preparation. **Yongkang Jin**: DFT calculations and manucript prepartion. **Benjamin L. Chen**: data analysis and manuscript prepartion. **Yan Wang**: data analysis and manuscript prepartion. **Lincoln Miara**: data analysis and manuscript prepartion. **Ryounghee Kim**: data analysis and manuscript prepartion. **Yan-Yan Hu**: conceptualization, data analysis, project supervision, and manuscript preparation.

Supporting Information

The supporting information contains quantitative analysis of the phase fractions from powder XRD and ^6Li NMR, ^{127}I NMR, ^{31}P NMR, impedance measurements, and AIMD simulations of glassy/crystalline Li_4PO_4I and glassy β- and γ-Li_3PO_4.

Declaration of Competing interest

The authors declare that they have no known competing financial interests or personal relationships that could have appeared to influence the work reported in this paper.

Acknowledgment

Supplementary materials

Supplementary material associated with this article can be found, in the online version, at doi:10.1016/j.ensm.2022.06.026.

References

[1] A. Manthiram, X. Yu, S. Wang, Lithium Battery Chemistries Enabled by Solid-State Electrolytes, Nature Reviews Materials 2 (4) (2017) 16103, https://doi.org/10.1038/natrevmats.2016.103.

[2] Q. Zhao, S. Stalin, C.-Z. Zhao, L.A. Archer, Designing Solid-State Electrolytes for Safe, Energy-Dense Batteries, Nature Reviews Materials 5 (3) (2020) 229–252, https://doi.org/10.1038/s41578-019-0165-5.

[3] Y. Zheng, Y. Yao, J. Ou, M. Li, D. Luo, H. Dou, Z. Li, K. Amine, A. Yu, Z. Chen, A Review of Composite Solid-State Electrolytes for Lithium Batteries: Fundamentals, Key Materials and Advanced Structures, Chem. Soc. Rev. (2020), https://doi.org/10.1039/D0CS00305K.

[4] L. Han, M.L. Lehmann, J. Zhu, T. Liu, Z. Zhou, X. Tang, C.-T. Heish, A.P. Sokolov, P. Cao, X.C. Chen, T. Saito, Recent Developments and Challenges in Hybrid Solid Electrolytes for Lithium-Ion Batteries, Frontiers in Energy Research 8 (2020) 202, https://doi.org/10.3389/fenrg.2020.00202.

[5] Z. Dong, C. Xu, Y. Wu, W. Tang, S. Song, J. Yao, Z. Huang, Z. Wen, L. Lu, N. Hu, Dual Substitution and Spark Plasma Sintering to Improve Ionic Conductivity of Garnet Li7La3Zr2O12, Nanomaterials 9 (5) (2019) 721, https://doi.org/10.3390/nano9050721.

[6] P. Wang, H. Liu, S. Patel, X. Feng, P.-H. Chien, Y. Wang, Y.-Y. Hu, Fast Ion Conduction and Its Origin in Li6–XPS5–XBr1+x, Chem. Mater. 32 (9) (2020) 3833–3840, https://doi.org/10.1021/acs.chemmater.9b05331.

[7] X. Feng, P.-H. Chien, S. Patel, Y. Wang, Y.-Y. Hu, Enhanced Ion Conduction in Li2.5Zn0.25PS4 via Anion Doping, Chem. Mater. 32 (7) (2020) 3036–3042, https://doi.org/10.1021/acs.chemmater.0c00025.

[8] L.S. Wang, S.V. Patel, S.S. Sanghvi, Y.-Y. Hu, S.M. Haile, Structure and Properties of Cs7(H4PO4)(H2PO4)8: A New Superprotonic Solid Acid Featuring the Unusual Polycation (H4PO4)+, J. Am. Chem. Soc. 142 (47) (2020) 19992–20001, https://doi.org/10.1021/jacs.0c08870.

[9] S.V. Patel, S. Banerjee, H. Liu, P. Wang, P.-H. Chien, X. Feng, J. Liu, S.P. Ong, Y.-Y. Hu, Tunable Lithium-Ion Transport in Mixed-Halide Argyrodites Li6–XPS5–XClBrx: An Unusual Compositional Space, Chem. Mater. 33 (4) (2021) 1435–1443, https://doi.org/10.1021/acs.chemmater.0c04650.

[10] I. Hanghofer, M. Brinek, S.L. Eisbacher, B. Bitschnau, M. Volck, V. Hennige, I. Hanzu, D. Rettenwander, H.M.R.Substitutional Disorder Wilkening, Structure and Ion Dynamics of the Argyrodites Li6PS5Cl, Li6PS5Br and Li6PS5I, Phys. Chem. Chem. Phys. 21 (16) (2019) 8489–8507, https://doi.org/10.1039/C9CP00664H.

[11] X. Feng, P.-H. Chien, Y. Wang, S. Patel, P. Wang, H. Liu, M. Immediato-Scuotto, Y.-Y. Hu, Enhanced Ion Conduction by Enforcing Structural Disorder in Li-Deficient Argyrodites Li6−xPS5−xCl1+x, Energy Storage Materials 30 (2020) 67–73, https://doi.org/10.1016/j.ensm.2020.04.042.

[12] X. Feng, P.-H. Chien, S. Patel, J. Zheng, M. Immediato-Scuotto, Y. Xin, I. Hung, Z. Gan, Y.-Y. Hu, Synthesis and Characterizations of Highly Conductive and Stable Electrolyte Li10P3S12I, Energy Storage Materials 22 (2019) 397–401, https://doi.org/10.1016/j.ensm.2019.07.047.

[13] H. Kageyama, K. Hayashi, K. Maeda, J.P. Attfield, Z. Hiroi, J.M. Rondinelli, K.R. Poeppelmeier, Expanding Frontiers in Materials Chemistry and Physics with Multiple Anions, Nature Communications 9 (1) (2018) 772, https://doi.org/10.1038/s41467-018-02838-4.

[14] J.-P. Malugani, R. Mercier, Vibrational Properties of and Short Range Order in Superionic Glasses AgPO3−AgX (X = I, Br, Cl), Solid State Ionics 13 (4) (1984) 293–299, https://doi.org/10.1016/0167-2738(84)90071-7.

[15] T. E. Kartini, Y.S. Panca Putra, I. Kuntoro, T. Sakuma, K. Basar, O. Kamishima, J Kawamura, Recent Studies on Lithium Solid Electrolytes (LiI)x(LiPO3)1-x for Secondary Battery Journal of the Physical Society of Japan 79 (Suppl.A) (2010) 54–58, https://doi.org/10.1143/JPSJS.79SA.54.

[16] N.H. Kaus, A.H. Ahmad, Conductivity Studies and Ion Transport Mechanism in LiI–Li 3 PO 4 Solid Electrolyte, Ionics 15 (2) (2009) 197–201.

[17] T. Asano, A. Sakai, S. Ouchi, M. Sakaida, A. Miyazaki, S. Hasegawa, Solid Halide Electrolytes with High Lithium-Ion Conductivity for Application in 4 V Class Bulk-Type All-Solid-State Batteries, Advanced Materials 30 (44) (2018) 1803075, https://doi.org/10.1002/adma.201803075.

[18] P.E. Blöchl, Projector Augmented-Wave Method, Phys. Rev. B 50 (24) (1994) 17953–17979, https://doi.org/10.1103/PhysRevB.50.17953.

[19] G. Kresse, J. Furthmüller, Efficient Iterative Schemes for Ab Initio Total-Energy Calculations Using a Plane-Wave Basis Set, Phys. Rev. B 54 (16) (1996) 11169–11186, https://doi.org/10.1103/PhysRevB.54.11169.

[20] J.P. Perdew, K. Burke, M. Ernzerhof, Generalized Gradient Approximation Made Simple, Phys. Rev. Lett. 77 (18) (1996) 3865–3868, https://doi.org/10.1103/PhysRevLett.77.3865.

[21] O.S. Oleneva, M.A. Kirsanova, T.A. Shestimerova, N.S. Abramchuk, D.I. Davliatshin, M.A. Bykov, E.V. Dikarev, A.V. Shevelkov, Trapping Phosphate Anions inside the [Ag 4I] 3+ Framework: Structure, Bonding, and Properties of Ag 4I(PO 4), Journal of Solid State Chemistry France 181 (2008) 37–44, https://doi.org/10.1016/j.jssc.2007.10.027.

[22] Y. Wang, W.D. Richards, S.P. Ong, L.J. Miara, J.C. Kim, Y. Mo, G. Ceder, Design Principles for Solid-State Lithium Superionic Conductors, Nature Materials 14 (10) (2015) 1026–1031, https://doi.org/10.1038/nmat4369.

[23] C.J. Pickard, F. Mauri, All-Electron Magnetic Response with Pseudopotentials: NMR Chemical Shifts, Phys. Rev. B 63 (24) (2001), 245101, https://doi.org/10.1103/PhysRevB.63.245101.

[24] J.R. Yates, C.J. Pickard, F. Mauri, Calculation of NMR Chemical Shifts for Extended Systems Using Ultrasoft Pseudopotentials, Phys. Rev. B 76 (2) (2007), 024401, https://doi.org/10.1103/PhysRevB.76.024401.

[25] Y.A. Du, N.A.W. Holzwarth, Li Ion Diffusion Mechanisms in the Crystalline Electrolyte γ-Li$_3$PO$_4$, Journal of The Electrochemical Society 154 (11) (2007) A999, https://doi.org/10.1149/1.2772200.

[26] N.D. Lepley, N.A.W. Holzwarth, Y.A. Du, Structures, Li$^+$ Mobilities, and Interfacial Properties of Solid Electrolytes Li$_3$PS$_4$ and Li$_3$PO$_4$ from First Principles, Phys. Rev. B 88 (10) (2013), 104103, https://doi.org/10.1103/PhysRevB.88.104103.

[27] C. Ibarra-Ramírez, M.E. Villafuerte-Castrejón, A.R.Continuous West, Martensitic Nature of the Transition SS→γ Li3PO4, Journal of Materials Science 20 (3) (1985) 812–816, https://doi.org/10.1007/BF00585719.

[28] V. Lacivita, N. Artrith, G. Ceder, Structural and Compositional Factors That Control the Li-Ion Conductivity in LiPON Electrolytes, Chem. Mater. 30 (20) (2018) 7077–7090, https://doi.org/10.1021/acs.chemmater.8b02812.

[29] G.O. Hartley, L. Jin, B.J. Bergner, D.S. Jolly, G.J. Rees, S. Zekoll, Z. Ning, A.T.R. Pateman, C. Holc, P. Adamson, P.G. Bruce, Is Nitrogen Present in Li3N·P2S5 Solid Electrolytes Produced by Ball Milling? Chem. Mater. 31 (24) (2019) 9993–10001, https://doi.org/10.1021/acs.chemmater.9b01853.

[30] N. Bloembergen, E.M. Purcell, R.V. Pound, Relaxation Effects in Nuclear Magnetic Resonance Absorption, Phys. Rev. 73 (7) (1948) 679–712, https://doi.org/10.1103/PhysRev.73.679.

[31] B. Stanje, H.M.R. Wilkening, Extremely Fast Interfacial Li Ion Dynamics in Crystalline LiTFSI Combined with EMIM-TFSI, ACS Phys. Chem Au 2 (2) (2022) 136–142, https://doi.org/10.1021/acsphyschemau.1c00032.

[32] J. Zheng, M. Tang, Y.-Y. Hu, Lithium Ion Pathway within Li7La3Zr2O12-Polyethylene Oxide Composite Electrolytes, Angewandte Chemie International Edition 55 (40) (2016) 12538–12542, https://doi.org/10.1002/anie.201607539.

[33] M.A.T. Marple, T.A. Wynn, D. Cheng, R. Shimizu, H.E. Mason, Y.S. Meng, Local Structure of Glassy Lithium Phosphorus Oxynitride Thin Films: A Combined Experimental and Ab Initio Approach, Angewandte Chemie International Edition 59 (49) (2020) 22185–22193, https://doi.org/10.1002/anie.202009501.

[34] B. Raguž, K. Wittich, R.Two New Glaum, Metastable Polymorphs of Lithium Pyrophosphate Li4P2O7, European Journal of Inorganic Chemistry 2019 (11–12) (2019) 1688–1696, https://doi.org/10.1002/ejic.201801100.

[35] K. Snyder, B. Raguž, W. Hoffbauer, R. Glaum, H. Ehrenberg, M. Herklotz, Lithium Copper(I) Orthophosphates Li3–XCuxPO4: Synthesis, Crystal Structures, and Electrochemical Properties, Zeitschrift für anorganische und allgemeine Chemie 640 (5) (2014) 944–951, https://doi.org/10.1002/zaac.201300606.

[36] J.G. Smith, D.J. Siegel, Low-Temperature Paddlewheel Effect in Glassy Solid Electrolytes, Nature Communications 11 (1) (2020) 1483, https://doi.org/10.1038/s41467-020-15245-5.